Observation of Spectral Structures in the Flux of Cosmic-Ray Protons from 50 GeV to 60 TeV with CALET on the ISS

Supplemental material relative to "Observation of Spectral Structures in the Flux of Cosmic-Ray Protons from 50 GeV to 60 TeV with CALET on the ISS."

DATA ANALYSIS

The event selection and analysis are carried out as in our previous publication [S1] with additional refinements and improvements. For instance, the charge selection with the IMC at high energies, which was not included in our previous publication, is now implemented. In the following we mainly discuss the new analysis procedures that have been introduced in this paper.

Charge Selection

Above a few TeV the CHD charge measurement is affected by a copious background generated by backscattered radiation and integrated along the length of the scintillator paddles and across their relatively wide lateral segmentation (2 cm). Instead, as can be seen in the examples of charge distributions given in Figure S1, below 2 TeV the background level is lower and we observe an excellent correlation of the IMC and CHD charge measurements. Above a few TeV, we take advantage of the high segmentation (1 mm) of the IMC fibers and apply charge cuts based only on the dE/dx information from the IMC fibers. In the main body of the paper, Figure 1 shows an example of the effectiveness of the IMC charge cut which is carried out by applying an energy-dependent selection, optimized via MC simulations, to give a constant efficiency of $\sim 98\%$. Charge selection based on the CHD signals uses a similar energy-dependent charge cut, albeit with a lower efficiency (close to 95%).
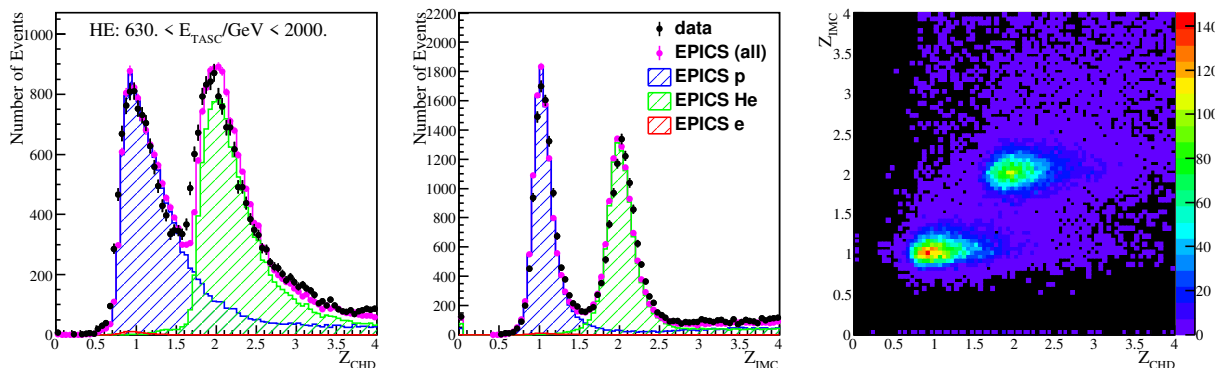
FIG. S1. Examples of charge distributions after applying criteria (1-7) (as explained in the main body of the paper) for CHD (left) and IMC (middle), and charge correlation plot (right) of IMC vs CHD. The events shown are selected with $630 < E_{\text{TASC}} < 2000$ GeV. The observed data are compared with the EPICS MC simulations.

Background Contamination

Background contamination is estimated from the MC simulations of proton, helium and electron events as a function of the observed energy by assuming their spectral shape as derived from previous measurements, i.e., AMS-02 [S2, S3] and CREAM-III [S4]. The dominant component of the contamination comes from off-acceptance protons except for the highest energy region above 5 TeV. For events taken with the HE-trigger, Figure S2 shows the background contamination, as a function of E_{TASC}, due to electron and helium events after removing the background from off-acceptance protons. The latter are efficiently removed by comparing the shower axis, as reconstructed in the TASC, with the direction of the track from the IMC. As can be seen in the figure, above 5 TeV the contamination is dominated by helium and its contribution ranges from a few % to 20% with a maximum in the highest energy region of $E_{\text{TASC}} \sim 20$ TeV corresponding to the primary proton energy of ~ 60 TeV. The effect of backscattering becomes increasingly more significant in this energy region. In the lower energy region covered by the LE-trigger, the total contamination, inclusive of off-acceptance protons, is suppressed and is lower than a few %. The larger contamination by helium above 5 TeV causes a significant contribution to the systematic errors as shown in Figure S2.

Energy Unfolding

Energy unfolding is adopted after subtraction of the background contamination as mentioned above. In this analysis, we use an unfolding method based on the Bayesian approach implemented in the RooUnfold package [S5, S6] in
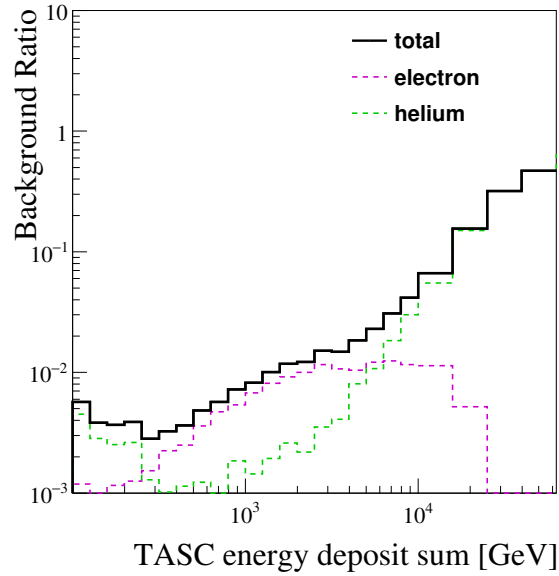
FIG. S2. Energy dependence of the background contamination due to the electron and helium contamination after subtracting off-acceptance protons (HE-trigger analysis).

ROOT [S7], with the response matrix derived from MC simulations. Convergence is obtained within two iterations, given the relatively accurate prior distribution obtained from the previous observations, i.e., by AMS-02 [S2] and CREAM-III [S4]. The energy spectrum obtained with the unfolding procedure is presented in Figure S3 and compared with the differential distribution of the TASC energy deposits as they were observed before the unfolding.
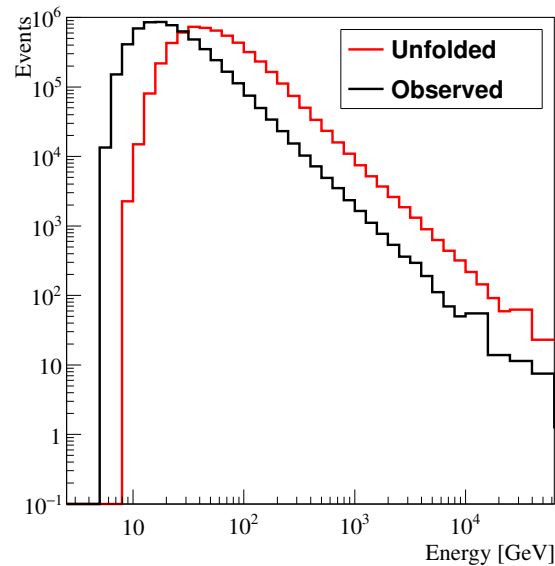
FIG. S3. Distribution of TASC energy deposits (Observed) after subtraction of the background contamination and the energy spectrum after the unfolding (Unfolded) in the HE-trigger analysis.

Consistency between LE and HE Analyses

The HE-trigger mode is always active on orbit to maximize the efficiency for high energy electrons above 10 GeV. For the data analysis, we applied an additional offline-trigger with a higher threshold to select events while avoiding the effects due to gain variations during the long observation period. Since the offline trigger threshold is higher than the one of the hardware trigger, the HE-trigger analysis introduces an efficiency bias at energies below 200 GeV, which is studied with a scan of the offline-trigger threshold using LE-trigger data. Therefore, LE-Trigger analysis is required below 200 GeV. As presented in Figure S4, the two spectra obtained with the LE and HE analyses are very well consistent in the energy region shared by the two analyses. They are combined around 300 GeV, taking into account the different statistics of the two trigger modes. As a result, the whole energy range from 50 GeV to 60 TeV has been observed by CALET.
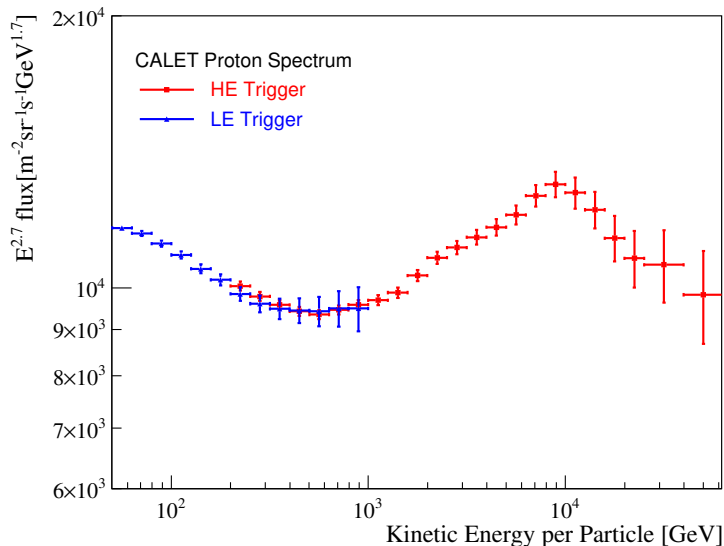
FIG. S4. Comparison of proton spectrum derived from two data sets corresponding to the HE-trigger (red) and LE-trigger (blue) analyses.

Systematic Uncertainties

Systematic uncertainties are estimated with LE and HE samples, respectively and shown in Figure S5 for the HE sample. Energy-independent systematic uncertainties are estimated around 4.1% in total, from the uncertainties on the live time (3.4%), long-term stability (1.4%), and radiation environment (1.8%). The latter contribution is mainly due to effects due to the ISS radiation environment. No time-dependent component due to the aging of the instrument is included in this category. Since low energy radiation rapidly increases in the polar region, these effects can be evaluated using the rigidity cutoff dependence of the observed spectrum. To study this uncertainty, flight data were divided into 4 cases of rigidity cutoff (Rc) range as (i) less than 2GV, (ii) 2-6GV, (iii) 6-10GV, and (iv) above 10GV. The systematic error due to ISS radiation environment was evaluated in the 20-100 GeV energy range resulting in a systematic uncertainty of 1.8%.

In addition to energy independent uncertainties, several sources of systematics are taken into account and shown separately, as a function of energy, in the same figure. They are denoted with the following labels: (1) "MC Model" for the dependence due to the uncertainties on the current models of hadronic interactions, (2) "TASC Hit Consistency", (3) "Shower Start in IMC", (4) "Charge ID" for the charge identification, (5) "Unfolding" for the energy response, and (6) "Beam Test Configuration". The uncertainty on the hadronic interaction models is estimated from the comparison of EPICS with GEANT4 and FLUKA. Contributions (2), (3), and (4) come from uncertainties on the event reconstruction. The uncertainty (5), stemming from the energy response, is estimated by summing up the energy deposits closest to the shower axis. We extrapolate the reconstructed track and determine its impact point on the TASC. By comparing different choices in the list of neighbor logs that we include in the sums

of deposits, we estimate the uncertainties associated to the measurement of the energy sum in the TASC due to the calorimeter granularity and to the shower width. An additional uncertainty (6) is estimated from the study of the difference between flight and beam test configurations. Details can be found in the Supplemental Material of [S1]. For $E < 10$ TeV, the overall uncertainty is less than 10%. For $E > 10$ TeV, the uncertainties from the MC model dependence and charge identification become large, reaching 30% at maximum.
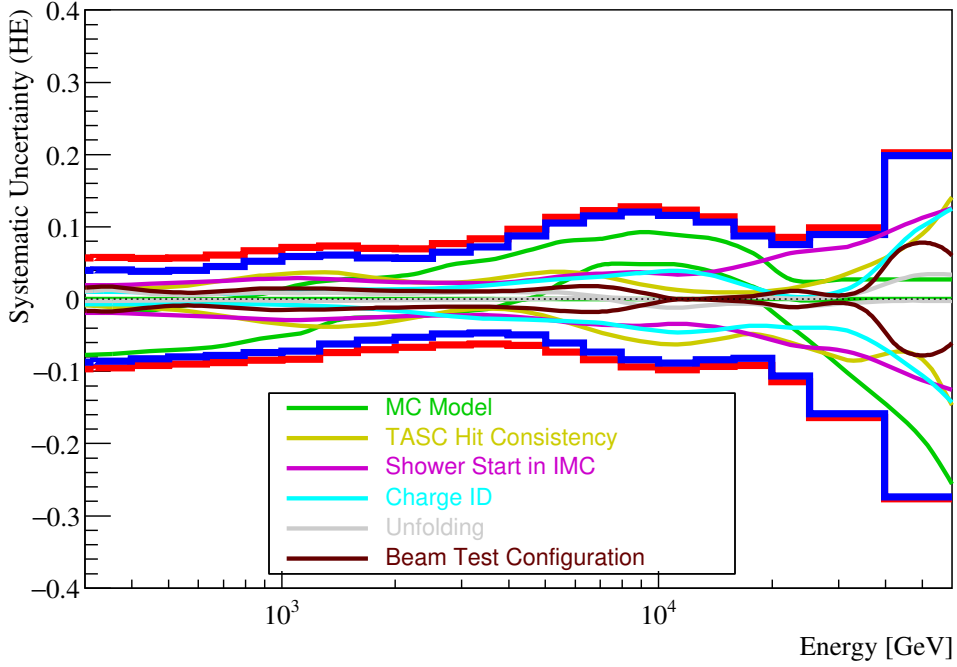
FIG. S5. Systematic uncertainties for the HE-trigger sample.

Results

The proton spectrum measured by CALET (red circles) is shown in Figure S6 where it is compared with the experimental results of AMS-02, CREAM-III, and DAMPE. The hatched band shows the total uncertainty for CALET. The dark blue colored band shows the total uncertainty for DAMPE.
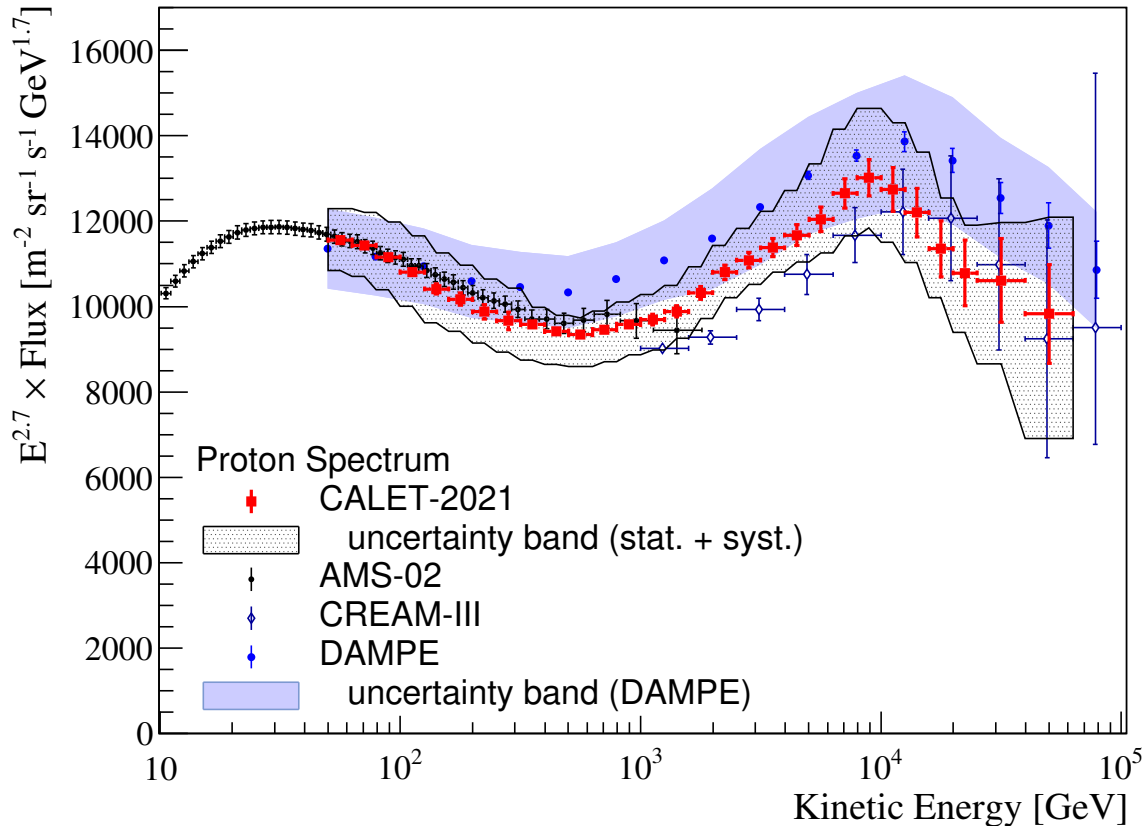
FIG. S6. Cosmic-ray proton spectrum observed with CALET from 50 GeV to 60 TeV using an energy binning with 10 bins per decade, except for the last two (wider) bins. The horizontal error bars are representative of the bin widths. The hatched band indicates the total uncertainty as the quadratic sum of systematic and statistical errors. Direct measurements in space by AMS-02 [S2], DAMPE [S8] and by balloon observation with CREAM [S4] are included for comparison. The dark blue band shows the total uncertainty for DAMPE.

Additional fit of the proton spectrum in energy sub-intervals

Separate fits of the proton spectrum, with single power-law functions, are shown in three different energy sub-intervals in Figure S7 where the error bars refer to purely statistical errors.
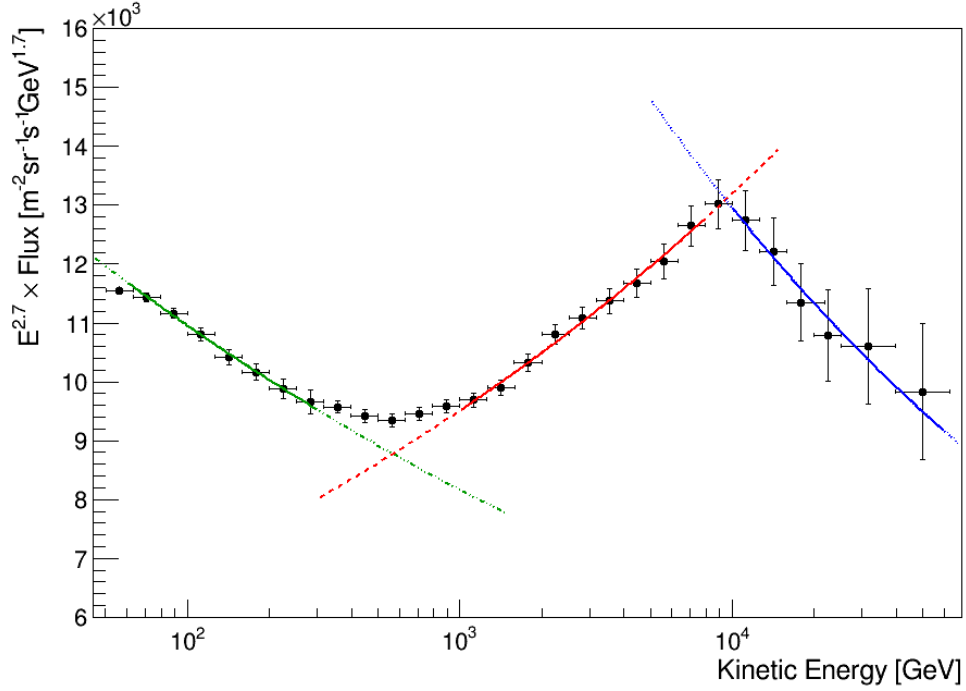
FIG. S7. Fits of CALET proton spectrum with single power-law functions. Green, red, and blue (solid) lines show the best fitted results in the energy intervals 60 – 300 GeV, 1 – 8 TeV, and 10 – 60 TeV. The corresponding fitted indices are -2.83 ± 0.02, -2.56 ± 0.01, and -2.89 ± 0.07, respectively. The values of $\Delta\gamma$ and $\Delta\gamma_1$ are consistent, within the errors, with the values obtained with the DBPL fit, as described in the main section of the paper.

TABLE I. CALET proton spectrum in tabular form. A representative energy value is evaluated for each bin from the geometric mean of the lower and upper edges. The first and second error associated with the bin energy represent the systematic error on the global energy scale and an energy dependent error, respectively. For the flux, the first, second and third error represent the statistical uncertainty (68% confidence level), a systematic uncertainty on the normalization, and an energy dependent systematic uncertainty, respectively.

Energy Bin (GeV)	Representative Energy (GeV)	Flux $(\mathrm{m}^{-2}\mathrm{sr}^{-1}\mathrm{s}^{-1}\mathrm{GeV}^{-1})$
$(5.01 - 6.31) \times 10^1$	$(5.62 \pm 0.16 \pm 0.06) \times 10^1$	$(2.18 \pm 0.01 \pm 0.09^{+0.10}_{-0.10}) \times 10^{-1}$
$(6.31 - 7.94) \times 10^1$	$(7.08 \pm 0.20 \pm 0.07) \times 10^1$	$(1.16 \pm 0.01 \pm 0.05^{+0.06}_{-0.06}) \times 10^{-1}$
$(7.94 - 10.00) \times 10^1$	$(8.91 \pm 0.25 \pm 0.09) \times 10^1$	$(6.06 \pm 0.05 \pm 0.25^{+0.36}_{-0.33}) \times 10^{-2}$
$(1.00 - 1.26) \times 10^2$	$(1.12 \pm 0.03 \pm 0.01) \times 10^2$	$(3.15 \pm 0.03 \pm 0.13^{+0.21}_{-0.19}) \times 10^{-2}$
$(1.26 - 1.59) \times 10^2$	$(1.41 \pm 0.04 \pm 0.01) \times 10^2$	$(1.63 \pm 0.02 \pm 0.07^{+0.11}_{-0.10}) \times 10^{-2}$
$(1.59 - 2.00) \times 10^2$	$(1.78 \pm 0.05 \pm 0.02) \times 10^2$	$(8.56 \pm 0.12 \pm 0.35^{+0.55}_{-0.50}) \times 10^{-3}$
$(2.00 - 2.51) \times 10^2$	$(2.24 \pm 0.06 \pm 0.02) \times 10^2$	$(4.46 \pm 0.08 \pm 0.18^{+0.27}_{-0.25}) \times 10^{-3}$
$(2.51 - 3.16) \times 10^2$	$(2.82 \pm 0.08 \pm 0.03) \times 10^2$	$(2.35 \pm 0.05 \pm 0.10^{+0.14}_{-0.13}) \times 10^{-3}$
$(3.16 - 3.98) \times 10^2$	$(3.55 \pm 0.10 \pm 0.04) \times 10^2$	$(1.25 \pm 0.01 \pm 0.05^{+0.05}_{-0.11}) \times 10^{-3}$
$(3.98 - 5.01) \times 10^2$	$(4.47 \pm 0.13 \pm 0.05) \times 10^2$	$(6.59 \pm 0.08 \pm 0.27^{+0.25}_{-0.54}) \times 10^{-4}$
$(5.01 - 6.31) \times 10^2$	$(5.62 \pm 0.16 \pm 0.06) \times 10^2$	$(3.51 \pm 0.04 \pm 0.14^{+0.14}_{-0.28}) \times 10^{-4}$
$(6.31 - 7.94) \times 10^2$	$(7.08 \pm 0.20 \pm 0.07) \times 10^2$	$(1.91 \pm 0.02 \pm 0.08^{+0.09}_{-0.15}) \times 10^{-4}$
$(7.94 - 10.00) \times 10^2$	$(8.91 \pm 0.25 \pm 0.10) \times 10^2$	$(1.04 \pm 0.01 \pm 0.04^{+0.05}_{-0.08}) \times 10^{-4}$
$(1.00 - 1.26) \times 10^3$	$(1.12 \pm 0.03 \pm 0.01) \times 10^3$	$(5.64 \pm 0.07 \pm 0.23^{+0.33}_{-0.41}) \times 10^{-5}$
$(1.26 - 1.59) \times 10^3$	$(1.41 \pm 0.04 \pm 0.02) \times 10^3$	$(3.09 \pm 0.04 \pm 0.13^{+0.19}_{-0.19}) \times 10^{-5}$
$(1.59 - 2.00) \times 10^3$	$(1.78 \pm 0.05 \pm 0.03) \times 10^3$	$(1.73 \pm 0.02 \pm 0.07^{+0.10}_{-0.10}) \times 10^{-5}$
$(2.00 - 2.51) \times 10^3$	$(2.24 \pm 0.06 \pm 0.04) \times 10^3$	$(9.74 \pm 0.15 \pm 0.40^{+0.55}_{-0.51}) \times 10^{-6}$
$(2.51 - 3.16) \times 10^3$	$(2.82 \pm 0.08 \pm 0.05) \times 10^3$	$(5.37 \pm 0.09 \pm 0.22^{+0.35}_{-0.26}) \times 10^{-6}$
$(3.16 - 3.98) \times 10^3$	$(3.55 \pm 0.10 \pm 0.06) \times 10^3$	$(2.96 \pm 0.06 \pm 0.12^{+0.21}_{-0.14}) \times 10^{-6}$
$(3.98 - 5.01) \times 10^3$	$(4.47 \pm 0.13 \pm 0.08) \times 10^3$	$(1.63 \pm 0.03 \pm 0.07^{+0.14}_{-0.08}) \times 10^{-6}$
$(5.01 - 6.31) \times 10^3$	$(5.62 \pm 0.16 \pm 0.10) \times 10^3$	$(9.03 \pm 0.22 \pm 0.37^{+0.95}_{-0.55}) \times 10^{-7}$
$(6.31 - 7.94) \times 10^3$	$(7.08 \pm 0.20 \pm 0.13) \times 10^3$	$(5.09 \pm 0.14 \pm 0.21^{+0.59}_{-0.37}) \times 10^{-7}$
$(7.94 - 10.00) \times 10^3$	$(8.91 \pm 0.25 \pm 0.17) \times 10^3$	$(2.81 \pm 0.09 \pm 0.12^{+0.34}_{-0.24}) \times 10^{-7}$
$(1.00 - 1.26) \times 10^4$	$(1.12 \pm 0.03 \pm 0.02) \times 10^4$	$(1.48 \pm 0.06 \pm 0.06^{+0.17}_{-0.13}) \times 10^{-7}$
$(1.26 - 1.59) \times 10^4$	$(1.41 \pm 0.04 \pm 0.03) \times 10^4$	$(7.61 \pm 0.36 \pm 0.31^{+0.81}_{-0.64}) \times 10^{-8}$
$(1.59 - 2.00) \times 10^4$	$(1.78 \pm 0.05 \pm 0.04) \times 10^4$	$(3.80 \pm 0.22 \pm 0.16^{+0.33}_{-0.31}) \times 10^{-8}$
$(2.00 - 2.51) \times 10^4$	$(2.24 \pm 0.06 \pm 0.05) \times 10^4$	$(1.94 \pm 0.14 \pm 0.08^{+0.15}_{-0.21}) \times 10^{-8}$
$(2.51 - 3.98) \times 10^4$	$(3.16 \pm 0.09 \pm 0.06) \times 10^4$	$(7.51 \pm 0.69 \pm 0.31^{+0.67}_{-1.19}) \times 10^{-9}$
$(3.98 - 6.31) \times 10^4$	$(5.01 \pm 0.14 \pm 0.10) \times 10^4$	$(2.01 \pm 0.24 \pm 0.08^{+0.40}_{-0.55}) \times 10^{-9}$

[S1] O. Adriani *et al.* (CALET Collaboration), Phys. Rev. Lett. **122**, [181102] (2019) .
[S2] M. Aguilar *et al.* (AMS Collaboration), Phys. Rev. Lett. **114**, 171103 (2015) .
[S3] M. Aguilar *et al.* (AMS Collaboration), Phys. Rev. Lett. **115**, 211101 (2015) .
[S4] Y. Yoon *et al.*, Astrophys. J. **839**, 5 (2017) .
[S5] T. Adye, in *arXiv:1105.1160v1* (2011) .
[S6] G. D'Agostini, *Nucl. Instrum. Methods Phys Res., Sect. A*, **362**, 487 (1995) .
[S7] R. Brun and F. Rademakers, *Nucl. Instrum. Methods Phys Res., Sect. A*, **389**, 81 (1997) .
[S8] Q. An *et al.* (DAMPE), Science Adv. **5**, eaax3793 (2019) .